

Fine-Tuned Global Neural Network Potentials for Global Potential Energy Surface Exploration at High Accuracy

Xin-Tian Xie, Tong Guan, Zheng-Xin Yang, Cheng Shang,* and Zhi-Pan Liu*



Cite This: *J. Chem. Theory Comput.* 2025, 21, 3576–3586



Read Online

ACCESS |



Metrics & More

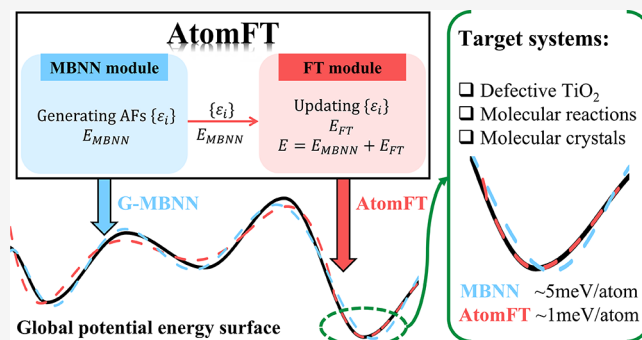


Article Recommendations



Supporting Information

ABSTRACT: Machine learning potential (MLP), by learning global potential energy surfaces (PES), has demonstrated its great value in finding unknown structures and reactions via global PES exploration. Due to the diversity and complexity of the global PES data set, an outstanding challenge emerges in achieving PES high accuracy (e.g., error <1 meV/atom), which is essential to determine the thermodynamics and kinetics properties. Here, we develop a lightweight fine-tuning MLP architecture, namely, AtomFT, that can explore PES globally and simultaneously describe the PES of a target system accurately. The AtomFT potential takes the pretrained many-body function corrected global neural network (MBNN) potential as the basis potential, exploits and iteratively updates the atomic features from the pretrained MBNN model, and finally generates the fine-tuning energy contribution. By implementing the AtomFT architecture on the commonly available CPU platform, we show the high efficiency of AtomFT potential in both training and inference and demonstrate the high performance in challenging PES problems, including the oxides with low defect content, molecular reactions, and molecular crystals—in all systems, the AtomFT potentials enhance significantly the PES prediction accuracy to 1 meV/atom.



1. INTRODUCTION

Machine learning potential (MLP) has become an indispensable tool in large-scale atomistic simulations, which offers a high computation efficiency for calculating large systems at an accuracy close to quantum mechanics (QM) calculations.¹ Despite years of efforts with many flavors of MLP models now available to both central processing unit (CPU) and graphic processing unit (GPU) hardware platforms,^{2–17} MLP remains to have two major deficiencies compared to QM calculations that can be freely applied to arbitrary systems: first, an MLP is often not available immediately for systems of interest due to the lack of a suitable data set for training;¹⁸ second, a high chemical accuracy (e.g., <5 meV) is generally difficult to achieve for structure-sensitive systems, particularly those involving long-range interactions and complex local reactions.^{19,20} In fact, current MLPs are mostly applied to specific systems with limited element types, mainly for extending the spatiotemporal scale of simulation on a local potential energy surface (PES), e.g., using molecular dynamics (MD). These deficiencies may be solved if a general-purpose and robust MLP with a massive parameter size is available by learning a comprehensive QM data set covering all elements and a diverse array of structures. The goal to generate such an all-purpose MLP is daunting, not least because of the huge challenges in obtaining a complete data set from QM calculations. It is thus desirable and more practical to develop a lightweight MLP architecture, which can achieve very high

precision for a target system and is also robust for global PES exploration.

It is now recognized that the completeness of a training data set is critical to the MLP transferability and thus the predictive ability. However, as the data set grows to include more and more diverse structures, not only does the training of MLP invoke substantial computational costs (training time and resource consumption), but the accuracy of MLP drops given the same MLP architecture. The global neural network (G-NN)^{21,22} potential in the large-scale atomic simulation using neural network potential (LASP) software,^{23–25} the MLP developed by our group and widely used by many users, provides a good example of this paradox. The G-NN is trained using the global PES data set from stochastic surface walking (SSW)^{26,27} global optimization and thus can be utilized for structure and reaction prediction in general. The energy accuracy of G-NN is typically around 6–10 meV/atom in root-mean-square error (RMSE).²⁸ As an upgrade of G-NN, the recently proposed many-body-function corrected neural net-

Received: January 12, 2025

Revised: March 6, 2025

Accepted: March 11, 2025

Published: March 19, 2025



work (MBNN),¹⁶ can further reduce the RMSE by half to 3–5 meV/atom in general for the global data set, e.g., with more than 100,000 structures. However, the MBNN architecture, following the high-dimension NN framework,⁷ is still a computationally less-intensive method: only atomic NN is utilized to achieve high efficiency on CPU hardware in training large data, and the computationally intensive atom-pair-based NN is avoided, although it should be able to improve the accuracy. For instance, the accuracy for a recently reported five-element Rh–Mn–C–H–O MBNN potential is 4.04 meV/atom, where the data set covers structures from all 31 different element combinations (5 one-element, 10 two-element, 10 three-element, 5 four-element, and 1 five-element).²⁹ While these G-(MB)NN potentials are able to reveal unexpected new chemistry on materials and catalytic reactions, they meet difficulties for PES tasks where the high accuracy (<1 meV/atom) is a must, to name a few, the evaluation of the defect energy in materials with low-content defects, the rate comparison between different chemical reactions, and the finding of the global minimum of molecular crystals.

The conflict between data completeness and MLP accuracy becomes even more obvious in recent implementations of universal graph NN MLPs on modern GPU devices.^{30–36} The performances of a few representatives are listed as follows. The M3GNet of 87 elements achieves an average energy prediction accuracy of 35 meV/atom with 227,549 parameters;³⁰ the CHGNet of 89 elements has the mean absolute error (MAE) accuracy of 30 meV per atom in energy and 77 meV/Å in force with 400,438 trainable parameters;³² MACE-MP-0 model of 104 elements achieves an energy MAE of 20 meV/atom and a force MAE of 45 meV/Å for the medium model with 4.69 million (M) parameters;³⁵ the DPA-2 MT model of 73 elements achieves a weighted average RMSE energy of 18.6 meV/atom and an RMSE force of 116 meV/Å with 7.68 M parameters.³⁶ The data sets utilized in different models are generally structure minima (not global PES data set) but from different sources. Although fine-tuning strategies may be utilized to improve the accuracy of these GPU models,³⁷ for example, a fine-tuned CHGNet model having 1.1 meV/atom energy MAE and 25.5 meV/Å force MAE on a Li₂ZrCl₆ test set,³² these models are heavy-weighted and lack of high efficiency in computation due to the complex MLP architectures with a large parameter size in the original universal model designed on GPU platform.

Herein, we develop a low-cost fine-tuning architecture, namely, atomic fine-tuning (AtomFT), executable on a CPU platform aiming for PES global exploration with a high accuracy at the target system. AtomFT is built on our previously developed MBNN architecture with a fine-tuning module to patch the PES via an additional energy contribution. The fine-tuning module implements a new set of many-body functions that exploit and iteratively update atomic features from the pretrained MBNN model. We show that the training of AtomFT potential has a low cost and can be utilized generally for challenging material and reaction systems with both high efficiency and high accuracy (~1 meV/atom).

2. METHODS

Our AtomFT architecture is designed to fine-tune the existing MBNN potential utilized in LASP simulation. The MBNN potential, trained on a global data set with diverse structure types and compositions, well balances the computation

efficiency and accuracy (e.g., RMSE 5 meV/atom) in PES global exploration, making it a qualified basis potential for fine-tuning. The AtomFT can improve the local PES description for the target system without destroying the global PES exploration ability of the basis MBNN potential.

As depicted in Figure 1, AtomFT consists of two parts: the base MBNN module (blue background) and the newly

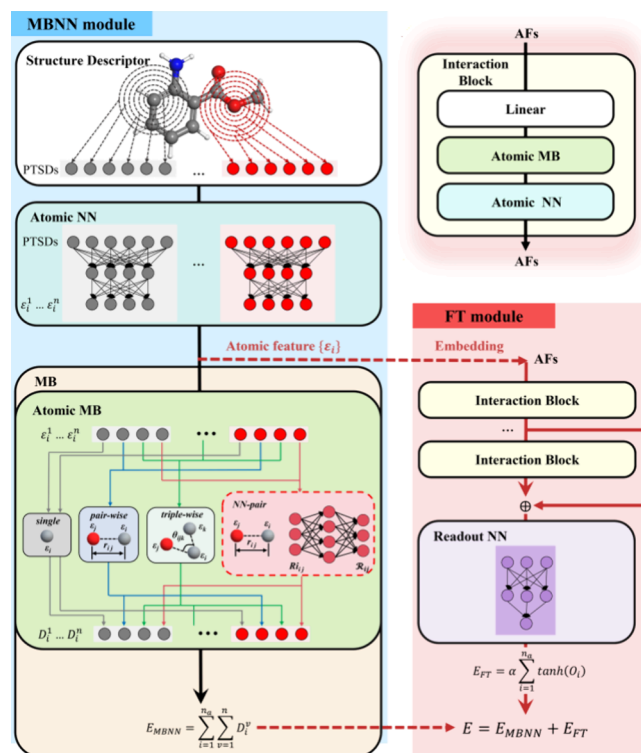


Figure 1. Illustration of the AtomFT architecture. The AtomFT contains the MBNN module (blue background) and the FT module (pink background). The MBNN module inherited from the MBNN architecture employs PTSD-input-based atomic NNs to generate atom-based coefficients that are used to compute MB functions and derive E_{MBNN} . The FT module, an extra fine-tuning module, takes atom-based coefficients from MBNN, the atomic features (AFs), as input and updates them iteratively through the interaction blocks (see the top-right inset). These AFs finally enter into a readout NN to produce an energy correction term, E_{FT} . The total energy of AtomFT is the sum of the two components.

implemented fine-tuning (FT) module (pink background). The MBNN module is inherited from the MBNN architecture; the fine-tuning module has a deep network structure, containing stackable interaction blocks and a readout NN block. The input of the fine-tuning module, the so-called atomic features (AF), comes from the atomic terms from MBNN, which are then iteratively updated by the deep network to yield the final energy correction term, E_{FT} . The total energy E is the sum of the original energy output from MBNN, E_{MBNN} , and correction E_{FT} .

$$E = E_{MBNN} + E_{FT} \quad (1)$$

By design, the data set for training AtomFT potential should be a small subset of local PES data, newly added to patch the global PES to enhance the target system's local accuracy. In the training of AtomFT, the parameters in the MBNN module are kept frozen, i.e., E_{MBNN} being constant), and only the

parameters associated with the fine-tuning module are updated. As both the training data set and parameter size are rather small, an efficient, low-cost global PES patching using AtomFT is thus achieved.

In the following subsections, we will first provide an overview of the MBNN architecture¹⁶ and then present the algorithm for the newly developed NN-type many-body (NN-MB) functions and finally the AtomFT architecture.

2.1. MBNN Architecture. The MBNN architecture, as shown in Figure 1 (blue background), utilizes the power-type structure descriptors (PTSDs)^{22,38} as the input for atomic NNs. Each atomic NN outputs a vector of n dimension, denoted as $\boldsymbol{\varepsilon}_i = \{\varepsilon_i^v, \text{ and } v = 1, 2, \dots, n\}$ for atom i , which is utilized to construct a set of explicit-function-type many-body (EF-MB) functions for yielding the atomic energies, D_i^v , shown in eq 2. Each atomic energy D_i^v corresponds to an atomic EF-MB f , and the total energy E_{MBNN} is the sum of D_i^v (eq 3), where λ is the hyperparameter; n_{MB}^i is the number of neighbor atoms of the central atom i in the cutoff radius, r_{MB} ; n_s , n_d , n_{sp} , and n_t correspond to the number of single-body, two-body, spherical harmonic, and three-body functions utilized in MBNN potential, respectively; and n_a is the number of atoms.

$$D_i^v = \begin{cases} \lambda f_s(\varepsilon_i^v), & 0 < v \leq n_s \\ \lambda \sum_{j=1}^{n_{\text{MB}}^i} f_d(\varepsilon_i^v, \varepsilon_j^v, r_{ij}), & n_s < v \leq n_s + n_d \\ \frac{1}{2} \lambda \sum_{m=-l}^l \left| \sum_{j=1}^{n_{\text{MB}}^i} f_{\text{sp}}(\varepsilon_i^v, \varepsilon_j^v, r_{ij}, m) \right|^2, & n_s + n_d < v \leq n_s + n_d + n_{\text{sp}} \\ \lambda \sum_{j=1}^{n_{\text{MB}}^i} \sum_{k=1}^{n_{\text{MB}}^i} f_t(\varepsilon_i^v, \varepsilon_j^v, \varepsilon_k^v, r_{ij}, r_{ik}, r_{jk}, \theta_{ijk}), & n - n_t \\ < v \\ \leq n \end{cases} \quad (2)$$

$$E_{\text{MBNN}} = \sum_{i=1}^{n_a} \sum_{v=1}^n D_i^v \quad (3)$$

$$f_s = \varepsilon_i^v \quad (4)$$

$$f_d = \varepsilon_i^v \varepsilon_j^v \frac{1}{r_{ij}^{m_d}} f_c(r_{ij}) \quad (5)$$

$$f_{\text{sp}} = \varepsilon_i^v \varepsilon_j^v r_{ij}^{m_{\text{sp}}} f_c(r_{ij}) Y_l^m(r_{ij}) \quad (6)$$

$$f_t = \varepsilon_i^v (\varepsilon_j^v + \varepsilon_k^v) \frac{(2 + \cos(\theta_{ijk}))^l}{r_{ij}^{m_t} \times r_{ik}^{m_t} \times r_{jk}^{m_t}} f_c(r_{ij}) f_c(r_{ik}) f_c(r_{jk}) \quad (7)$$

$$f_c(r_{ij}) = \begin{cases} \tanh^3 \left[1 - \frac{r_{ij}}{r_{\text{MB}}} \right], & r_{ij} \leq r_{\text{MB}} \\ 0, & r_{ij} > r_{\text{MB}} \end{cases} \quad (8)$$

Specifically, the forms of the EF-MB functions, including single-body function (f_s), two-body function (f_d), sphere harmonic function (f_{sp}), and three-body function (f_t) are

expressed in eqs 4–7. These functions are the numerical representations of coordinates, as inspired by the classical force fields in describing the physical interactions, where f_c in all equations is the cutoff function (eq 8) with a cutoff radius r_{MB} , and Y_l^m is the spherical harmonic at degree l and order m . Notably, the sphere harmonic function f_{sp} can be regarded as a special type of two-body function. In these functions, all power parameters ($m_d, m_{\text{sp}}, m_t, l_t$), the cutoff (r_{MB}), and the degree of spherical harmonics (l) are hyperparameters, which are set as input in training the MBNN potential.

2.2. NN-Type Many-Body Functions. In this work, to achieve a high performance in AtomFT, we propose a new type of MB function, namely NN-MB functions, which are analogs to the EF-MB functions except that the radial parts in EF-MB functions are replaced by the output from a pair-based neural network (pair NN), being a vector $\mathcal{R}_{ij} = \{\mathcal{R}_{ij}^u, u = 1, 2, \dots, n_{\text{MB}}\}$ with a dimension of n_{MB} for ij pair. For example, eqs 9 and 10 give the formula of the two-body f_{Nd} (eq 9) and the spherical harmonics f_{Nsp} (eq 10) NN-MB, respectively, which utilize \mathcal{R}_{ij}^u from the pair NN as the radial parameter. The atomic pair NN is computationally intensive, being common in MLP on GPU hardware but not implemented on CPU hardware previously.

This pair NN takes the information on the atomic pair (atom i, j) as the input, including the atomic number (z_i and z_j) and the pair distance (r_{ij}), as shown in eqs 11–13, where k is the index of the input vector $Ri_{ij} = \{Ri_{ij}^k, k = 1, 2, \dots, n_R\}$ with a dimension n_R . By design, most of the elements ($k > 5$) are the Gaussian basis discretization of the pair distance r_{ij} , each associated with a fixed center, s_k , incremental from 0.5 to the cutoff radius r_{MB} . The δ of the Gaussian function is a hyperparameter, typically being 0.002. In this work, only two-body NN-MB (eq 9) is utilized for generating AtomFT potentials for a balance of efficiency and accuracy.

$$f_{\text{Nd}} = \varepsilon_i^v \varepsilon_j^v \mathcal{R}_{ij}^u f_c(r_{ij}) \quad (9)$$

$$f_{\text{Nsp}} = \varepsilon_i^v \varepsilon_j^v \mathcal{R}_{ij}^u f_c(r_{ij}) Y_l^m(r_{ij}) \quad (10)$$

$$\mathcal{R}_{ij} = \text{NN}\{\mathbf{Ri}_{ij}\} \quad (11)$$

$$Ri_{ij}^k(z_i, z_j, r_{ij}) = \begin{cases} 0.01 \max(z_i, z_j), & k = 1 \\ 0.01 \min(z_i, z_j), & k = 2 \\ \frac{1}{r_{ij}^{k-2}}, & 2 < k \leq 5 \\ e^{-(r_{ij}-s_k)^2/\delta}, & 5 < k \leq n_R \end{cases} \quad (12)$$

$$s_k = \frac{(r_{\text{MB}} - 0.5)(k - 6)}{n_R - 6} + 0.5 \quad (13)$$

2.3. AtomFT Architecture and FT Module. The AtomFT architecture inherits the MBNN module and adds the FT module (pink background). The output of the atomic NN from the MBNN module, $\{\varepsilon_i\}$, serves as the initial AFs, embedding the atomic structural features learned from the global data set. The interaction blocks are then utilized for updating AFs, and following the standard architecture in deep networks, we couple different interaction blocks using the residual operation, where the output of each preceding interaction block adds to the output of the current block.

This iterative procedure of AF updates ends with a readout NN to yield the final fine-tuning energy, E_{FT} .

Each interaction block comprises sequentially three sub-blocks, namely, linear layers, atomic MB functions, and atomic NNs. Trainable parameters in the FT module are present in the linear layers and the atomic NNs. The linear layers are used to rescale AFs to generate the coefficients for atomic MB functions. The atomic MB functions, as described in eq 2, further envelop the essential structural information into AFs and expand the perceptible range of the chemical environment for the current atom. The subsequent atomic NN introduces the nonlinearity and develops the complexity of the AFs. Obviously, after passing through every additional interaction block, the geometrical scope of AFs extends by a cutoff range of r_{MB} . While AFs are iteratively updated, the radial part of the atomic MB functions remains the same and thus can be saved for use after a first-time calculation. The idea of the interaction blocks and the iterative updating scheme is somewhat similar to the message-passing neural network (MPNN) scheme implemented on the GPU platform,¹⁰ but AtomFT takes complex AFs from MBNN as input and can incorporate conveniently different MB functions, each with different cutoffs, which facilitates to achieve a high PES accuracy without using many interaction blocks (see Section 3 below).

In the final part of the FT module, a readout NN is employed to generate the atomic fine-tuning energy, which is then summed over all atoms to yield E_{FT} . Since the FT module aims to patch the total energy from MBNN, i.e., E_{FT} should be a small quantity within a few tenth eV per atom, it should be possible to confine the output of readout NN, O , using a tanh function, as written in eq 14. An adjustable parameter, α , is utilized to control the magnitude of the output. Indeed, from our testing examples, the typical value of α should be in a range of 0.10 to 0.40 eV, consistent with our expectation of the maximum PES error from MBNN potential.

$$E_{\text{FT}} = \alpha \sum_{i=1}^{n_a} \tanh(O_i) \quad (14)$$

3. RESULTS AND DISCUSSION

3.1. Efficiency on the AtomFT Potentials. As our AtomFT architecture aims to fine-tune a local data set with a small size, the training cost is generally much lower compared to that required to train the basis potential. This can be seen in Figure 2a,b, where the AtomFT training is performed in two representative systems, a binary Ti–O system where the fine-tuning data set consists of bulk TiO_x , and a quaternary C–H–O–N system where the fine-tuning data set is from molecular crystal structures. Table 1 provides all the details on the MBNN and AtomFT architectures of two potentials and the information on the data sets (also see Supporting Information (SI) Parts 1 and 2).

The basis MBNN potentials are newly trained on the global data sets of 27,279 structures for Ti–O and 126,191 for C–H–O–N (Table 1) obtained from LASP G-NN library (<http://www.lasphub.com/#/lasp/nnLibrary>), where the total number of atomic MB utilized is 45, including one single-body, 20 two-body, 8 three-body, and 16 NN-type two-body terms. For reference, the Ti–O MBNN basis potential was trained parallelly on 1,536 CPU cores (Intel(R) Xeon(R) Platinum 8168 CPU), taking 20,000 epochs with each epoch 1.15 s; the C–H–O–N MBNN basis potential was on a 3,072

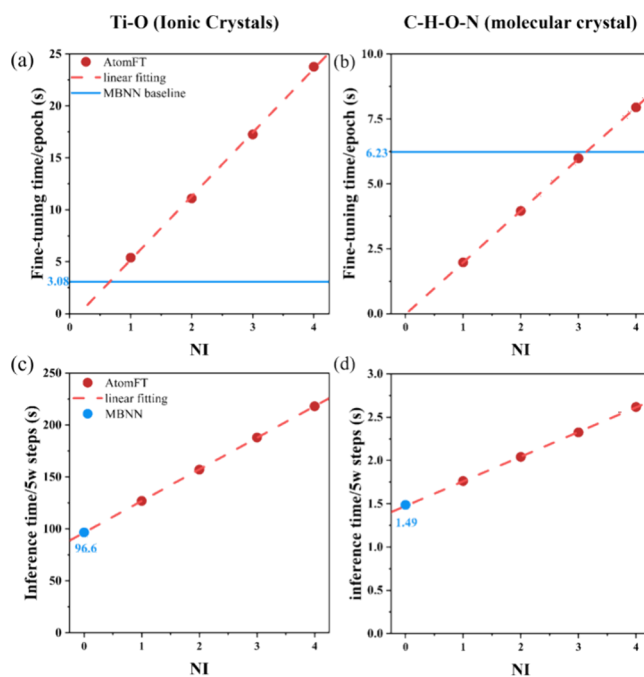


Figure 2. Fine-tuning (top panel) and inference (bottom panel) time of the AtomFT potentials with the number of interaction blocks (NI) from 1 to 4 for Ti–O ionic crystal (a, c) and C–H–O–N molecular crystal (b, d) systems. The time for the corresponding MBNN potentials calculated on fine-tuning and inference data sets is marked as blue lines and dots, respectively. The fine-tuning phase is conducted on a 96-core CPU machine, and the inference phase is conducted on a 24-core CPU machine (Intel(R) Xeon(R) Platinum 8168 CPU).

CPU cores, taking 30,000 epochs with each epoch 5.65 s. The final RMSE accuracy of energy and forces for the training set is 5.008 meV and 0.122 eV/Å for Ti–O and 5.406 meV/atom and 0.167 eV/Å for the C–H–O–N MBNN potentials. It might be mentioned that the utilization of many MB functions, particularly NN-type MB functions, does improve the accuracy of the MBNN potentials. For example, the RMSE of energy of the previous MBNN using only 5 MB functions is 5.76 meV/atom,¹⁶ being 0.75 meV/atom larger than the current version (more details on global data sets and MBNN training can be found in the SI Part 2).

Building upon the two MBNN basis potentials, we then fine-tune the two systems using a small fine-tuning data set to test the fine-tuning efficiency of the AtomFT framework. The two data sets, as listed in Table 1, are as follows: Ti–O with 200 bulk TiO_x structures generated by MD simulations on defective TiO_x structures, each with 196 atoms, and C–H–O–N with 1,400 molecular crystal structures generated by SSW global PES exploration of a 40-atom crystal. Up to four interaction blocks are utilized in AtomFT to examine the scaling with respect to the network depth. After fine-tuning, PES calculation of the AtomFT potentials, also generally known as the inference of the machine learning model, is performed. The timing of the AtomFT potential for the training and inference is collected and plotted in Figure 2.

Figure 2a shows that with the increase of the number of interaction blocks (NI), i.e., from 1 to 4, the fine-tuning train cost increases linearly (the red dotted line) from 5.39 to 23.77 s per epoch. The dominant time is spent on atomic MB calculations due to the pairwise operation in computing NN-

Table 1. Information on the Ti–O and C–H–O–N Potentials and the Performance of the AtomFT Potentials^a

		Ti–O	C–H–O–N		
MBNN architecture	MBNN Atomic NN	173–128–128–80–45	535–144–144–144–45		
	number of MB functions*	45	45		
	pair NN	64–64–64–16	64–64–64–16		
	number of parameters	114986	511236		
AtomFT architecture	linear layers	45–80–45	45–80–45		
	atomic NN	45–80–80–45	45–80–80–45		
	readout NN	45–144–80–1	45–80–80–1		
	number of parameters	42260NI + 18305	84520NI + 10241		
MBNN potential	global data set size**	27,279	126,191		
	RMSE for energy (meV/atom)	5.008	5.406		
	RMSE for force (eV/Å)	0.122	0.167		
efficiency	fine-tuning data set size	200	1,400		
accuracy	example ID	1	2	3	
	NI	1	2	1	1
	α	0.10	0.10	0.40	0.20
	sampling method	MD	MD	DESW	SSW
	fine-tuning data set size	410	410	689	1,900
	fine-tuning RMSE for energy (meV/atom)	0.600	0.436	0.169	0.814
	fine-tuning RMSE for force (eV/Å)	0.080	0.069	0.011	0.048
	testing data set size	42	42	63	222
	testing RMSE for energy (meV/atom)	0.829	0.768	0.291	0.976
	testing RMSE for force (eV/Å)	0.088	0.085	0.030	0.052

^aListed data includes the network description of the MBNN basis potential and AtomFT potential, MBNN potential global dataset size and accuracy, and detailed information on the efficiency and accuracy assessments of AtomFT potentials. 45 MB functions are constituted by one single-body, 20 two-body, 8 three-body, and 16 NN-two-body terms. *The MB function hyperparameters are detailed in *SI Part 1*. **More global data set information can be found in *SI Part 2*.

type MB functions, whereas all NN calculations take less than 18% of the total time. For reference, the MBNN basis potential is also trained using the same fine-tuning data set, and the time required is 3.08 s per epoch (the baseline in *Figure 2a*), which is lower than the fine-tuning time. Similarly, for the molecular crystal system shown in *Figure 2b*, the fine-tuning cost also increases linearly (the red dotted line) from 1.97 to 7.94 s per epoch with the NI increasing from 1 to 4. The training of MBNN basis potential takes 6.23 s, which is about the time for training AtomFT with NI = 3. This is apparently because the atomic NN in MBNN is large and has four elements (see *Table 1*), leading to a large size of trainable parameters (511236). From the above fine-tuning results, we can conclude that the cost for training an AtomFT potential is at least two or 3 orders of magnitude lower than training the MBNN basis potential considering that the global data set utilized for training MBNN is typically much larger (e.g., 100 times, see *Table 1*) than the fine-tuning data set.

For the PES calculation of the AtomFT potentials, the inference time is also linear with the NI, as shown in *Figure 2c,d* for both systems. The time is measured using a large system (768-atom structure for Ti–O; 720-atom for C–H–O–N) with repeated 50,000 energy/force evaluations. For comparison, the MBNN computational time, t_{MBNN} (being equivalent to NI = 0) is also included (the blue dot) in the figure. It shows that the additional time for the fine-tuning module scales with a slope of 0.20–0.30 t_{MBNN} as a function of NI. Apparently, the atomic NN block in the MBNN block, having a large number of NN parameters, remains the major bottleneck in the inference with small NI, being at most 60% when NI \leq 2. This relation suggests that a large NI is computationally expensive on the CPU platform and should be avoided in practice. In fact, in the following sections, we will

show that NI = 1 is already enough for most applications thanks to the good transferability of MBNN basis potential, offering AtomFT as a low-cost but powerful approach to enhancing PES accuracy.

3.2. Accuracy of the AtomFT Potentials. The primary objective of AtomFT is to significantly enhance the accuracy of the local PES description. To achieve this goal, we select three representative systems to assess the performance of the AtomFT potential: (i) oxides with low defect content; (ii) chemical reactions; and (iii) molecular crystals. These systems correspond to three distinct types of PES challenges, namely, long-range interactions between ionic defects, complex local covalent interactions for accurately describing reaction barriers, and weak van der Waals interactions necessary for distinguishing molecular crystal phases. Three example systems are constructed accordingly using the aforementioned Ti–O and C–H–O–N MBNN potentials (details of the potentials listed in *Table 1* top panel). The AtomFT performance of these systems is elaborated in the following.

Example 1: Defective TiO₂ Bulk and Surfaces. As shown in our previous work, TiO₂ oxides with anion and/or cation vacancies are poorly described by the atomic NN architecture and thus serve as good examples to examine the long-range interactions due to defects.¹⁶ In this work, we conduct both static and dynamic calculations on several defective TiO₂ systems with different situations for long-range interactions.

For the static calculation sample, 10 different defective TiO₂ rutile structures, including both bulk and surface structures, are chosen as the models, as illustrated in *Figure 3a*. These defective bulk structures are constructed from a rutile TiO₂ crystal bulk (192 atoms) by removing a number of O and Ti atoms. The surface slab models are generated from a rutile TiO₂ (110) surface slab model (180 atoms) by removing or

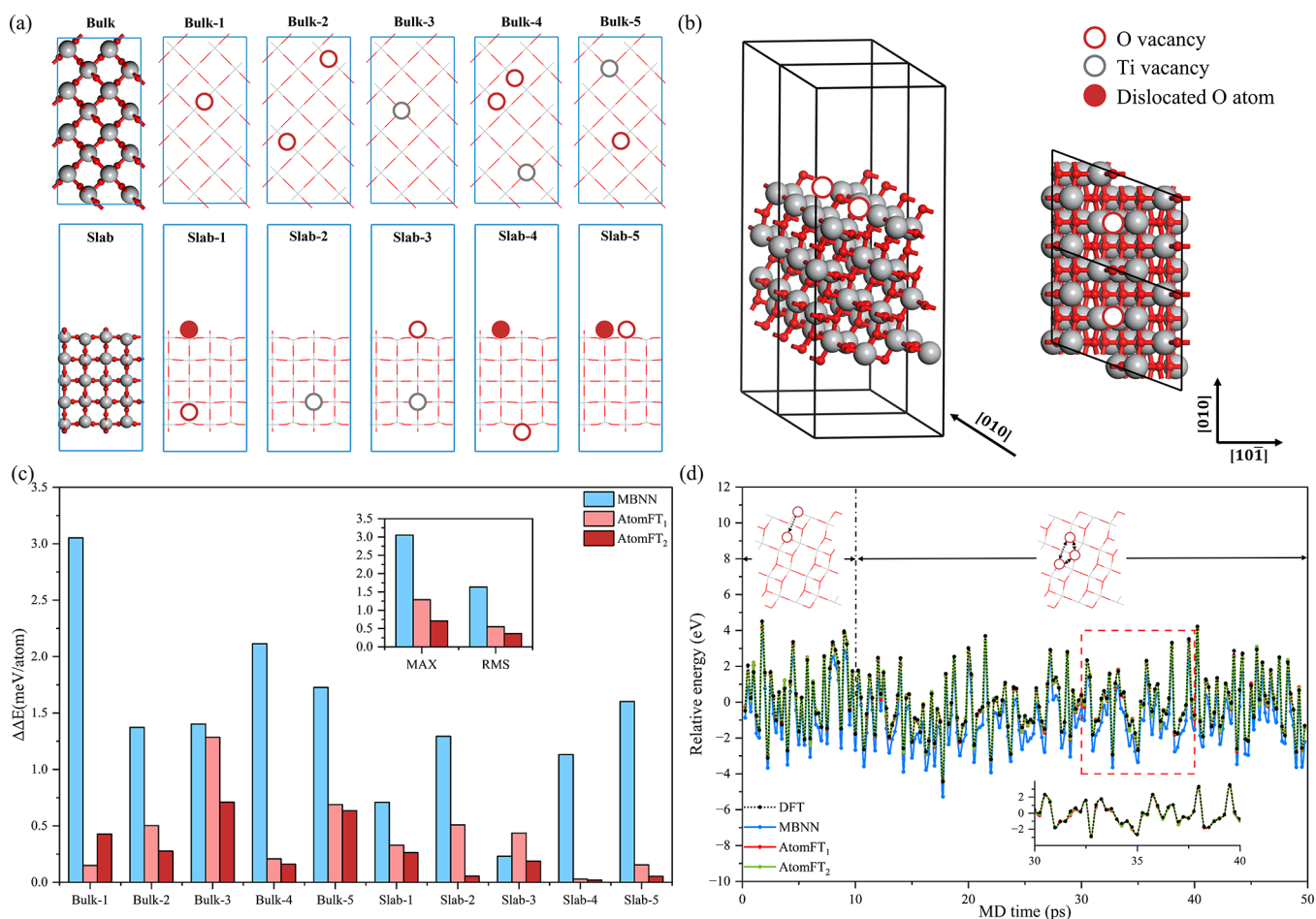


Figure 3. Performance of AtomFT potential in defective TiO₂ bulk and surface systems. (a) Ten defective rutile TiO₂ bulk and surface (slab model) structures along with the perfect structures on the left. (b) Side and top views of anatase TiO₂(101) with a surface O vacancy, which serves as the initial structure in MD simulation. (c) Error of the defect formation energy ($\Delta\Delta E$) of MBNN, AtomFT₁, and AtomFT₂ potentials for different defective structures. The absolute max errors and RMSE values of ΔE of the ten structures are shown in the inset. (d) Variation of the computed energy using DFT, MBNN, AtomFT₁, and AtomFT₂ potentials along the O vacancy migration trajectory, where all energies are shifted with respect to the average energy of the DFT trajectory, energy zero. The RMSE values are 9.07 meV/atom for MBNN, 1.83 meV/atom for AtomFT₁, and 1.62 meV/atom for AtomFT₂. The inset structures (top panel of (d)) highlight the change of the position of the vacancy (hollow circle), and the inset at the bottom is an enlarged window, showing the overlap between AtomFT and DFT results.

displacing the O and/or Ti atoms. For the dynamic calculation sample, an anatase TiO₂ (101) surface slab with a surface O vacancy is utilized as the initial model (Figure 3b), where the surface O vacancy is known to propagate into bulk above 200 K.³⁹ The AtomFT training is performed over a data set of 410 structures, randomly selected from finite temperature MD trajectories of these target structures (1.0 ps for each static sample structure and 50 ps for the dynamic sample) using the MBNN basis potential. The NI values of 1 or 2 are utilized to generate the AtomFT potentials, denoted as AtomFT₁ or AtomFT₂. We have carefully evaluated the performance of AtomFT with different NI values, and NI values below 2 generally achieve the best performance, as discussed in SI Part 3.

By using AtomFT₁ and AtomFT₂, the defect formation energy (ΔE), the energy difference between the optimized defect and the perfect structures, is computed, and the error between the AtomFT potential and DFT ($\Delta\Delta E$) is obtained. Figure 3c displays the absolute max errors and RMSE values for ΔE of the ten defective structures (Figure 3a). It shows that the $\Delta\Delta E$ decreases significantly as NI increases. The RMSE drops from 1.63 meV/atom of MBNN basis potential to 0.55

meV/atom of AtomFT₁ and 0.36 meV/atom of AtomFT₂, reaching less than one-fourth of the MBNN error. This indicates that AtomFT can systematically improve the long-range interaction description of different defect formations. We note that only bulk structures with multiple defects, i.e., bulk-3 and bulk-5 (Figure 3c), remain to have relatively larger errors at the AtomFT₂ level, which should be attributed to the low data population of these high-content defects in the whole data set.

To assess the dynamic properties, we perform a high temperature (1600 K) MD starting from the anatase (101) with a surface O vacancy using the AtomFT₁ potential. The MD simulation utilizes the canonic ensemble (NVT using the Nosé–Hoover algorithm)⁴⁰ as implemented in LASP with a time step of 0.5 fs and a total time of 50 ps. The energy is conserved well, fluctuating within only 0.0056 meV/atom. During the MD simulation, the oxygen vacancy migrates from the surface layer to the subsurface and then jumps frequently between the subsurface layer positions (see Figure 3d insets).

By collecting structures at an interval of 0.25 fs from the MD trajectory, we then evaluated their single-point energies using DFT (PBE functional), MBNN, AtomFT₁, and AtomFT₂

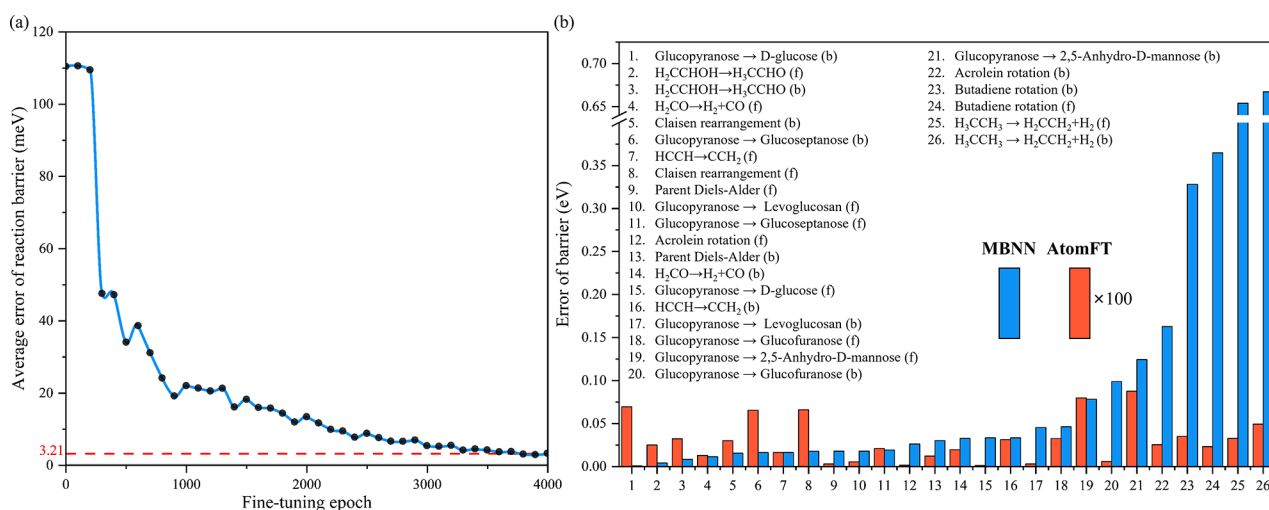


Figure 4. Performance of AtomFT potential in molecular reactions. (a) Average error of the reaction barrier in 26 reactions at different epochs along the fine-tuning learning curve. (b) Error of the reaction barrier for 26 reactions from MBNN and AtomFT potentials compared with the DFT barrier. In the figure, the error from AtomFT is enlarged by 100 times. The reactions are listed in the top-left corner of the figure, where (f) and (b) indicate the forward and backward reaction. The reactions are ranked according to the error of the MBNN results.

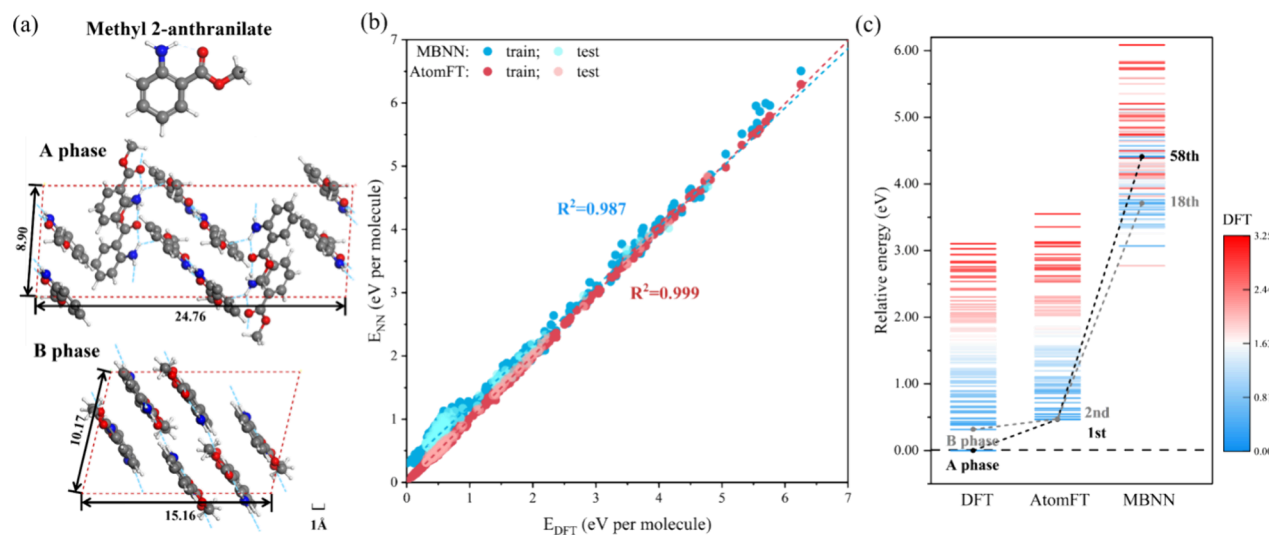


Figure 5. Performance of AtomFT potential in molecular crystals. (a) Structures of the methyl 2-anthranilate molecule, the two crystal phases (A and B phases). (b) Scatter plot illustrating the correlation between energies calculated using NN potentials (MBNN and AtomFT) and DFT for the training and the testing data sets (see Table 1, the accuracy rows). (c) Energy spectrum for 95 low-energy crystal structures (12 molecules per cell) using DFT, AtomFT, and MBNN models. The ranks of the A and B phases are marked in the figure. For (b) and (c), all energies are shifted such that the lowest DFT energy is zero.

potentials. Figure 3d shows the variation of the energies along the simulation time, with all energies being relative to the average energy from DFT data (energy zero). It shows that the energy curves of the AtomFT potentials and DFT overlap highly, as reflected from the zoomed-in window (Figure 3d inset). The RMSE of energy for the trajectory is 1.83 meV/atom for AtomFT₁, and 1.62 meV for AtomFT₂, being much lower than the 9.07 meV/atom for the MBNN potential (blue curve in Figure 3d).

Example 2: Molecular Gas-Phase Reactions. Following our previous work, we select 13 distinct molecular gas-phase reactions from the Baker test system and glucose decomposition studies as models to examine the accuracy of the reaction barrier calculations.^{41,42} These reactions encompass various types of local chemical bond rotation/making/breaking, such as isomerization, ring transformations, dehy-

drogenations, and rearrangements. More details on the reactions can be found in SI Part 4.

By applying the double-ended surface walking (DESW) transition state search method⁴³ to scan the reaction pathway for the 13 reaction pairs, we generate the fine-tuning data set by randomly selecting 752 structures from the pathways, which are split into the training set (689 structures) and the test set (63 structures). The AtomFT potential with NI = 1 is then trained, and as shown in Figure 4a, we plot the average value for the absolute error of barrier in 26 reactions, including both forward and backward reactions, against the fine-tuning epoch number. It shows that the average error of barriers drops rapidly from the initial 110.5 meV of the MBNN basis potential to below 10 meV after 2,000 epochs and finally flattens at ~4000 epochs, reaching 3.21 meV. The relatively large deviation of MBNN in the reaction barrier, e.g.,

exceeding 100 meV, could lead to large errors in assessing reaction kinetics due to the exponential dependence of reaction rate on barrier height.⁴⁴

Figure 4b further analyzes the barrier error for each reaction using the final AtomFT potential (4,000 epochs), showing the absolute reaction barrier difference between AtomFT potential and DFT compared with that between MBNN potential and DFT, where the AtomFT results are enlarged by a factor of 100 to compare with the MBNN results. The reactions are ranked according to the error of the MBNN results. All data are included in SI Part 4. The reaction barrier discrepancy for each reaction is no more than 9 meV using the AtomFT potential, about 1% of the error using the MBNN potential. We note that this improvement is especially pronounced in reactions such as butadiene rotation from the *s-cis* conformer to the *s-trans* conformer and ethylene hydrogenation, where the MBNN potential exhibits deviations exceeding 300 meV, which typically means the lack of relevant reaction data (low data density) in the original training set. The significant improvement of AtomFT calculations across all target reactions indicates that the reaction barrier prediction is very sensitive to the data set completeness, and the fine-tuning of a target reaction data set is a low-cost measure to quickly improve the reaction PES accuracy.

Example 3: Molecular Crystals. Methyl 2-anthranilate, a molecule with the chemical formula $C_8H_9NO_2$ (Figure 5a), has only one known experimental crystal structure and is selected by the seventh blind test of crystal structure prediction⁴⁵ (in the entry of XXIX) to challenge theoretical methods for structure prediction. This observed crystal structure, denoted as A phase, has a $P2_1/c$ space group, containing 12 molecules per cell (240 atoms), arranged in three symmetry-independent molecules.⁴⁶ In the structure of the A phase, the amino and ester functional groups of molecules form both intermolecular and intramolecular hydrogen bonds: there are 28 hydrogen bonds per cell (Figure 5a). A major challenge to identifying the correct crystal phase from theory is to accurately predict the total energy of different crystal phases.

By using SSW method to explore the crystal PES with variable supercell size, we sampled 2,122 structures from over 200,000 configurations, which contain 1,522 two-molecule, 50 four-molecule, 100 six-molecule, 100 eight-molecule, 100 ten-molecule, and 250 twelve-molecule structures. The fine-tuning based on the C–H–O–N MBNN potential with NI = 1 is performed on the training data set (1,900 structures), and the remaining 222 structures are utilized as the test sets. Figure 5b compares the performance of the C–H–O–N potential before (MBNN) and after the fine-tuning (AtomFT) on the training and test data sets, by correlating the total energies per molecule calculated by the MBNN, AtomFT potentials, and DFT with the PBE functional. Since XXIX molecule and crystals are totally absent in the C–H–O–N global data set, its RMSE of energy, being 11.07 meV/atom from MBNN, is acceptable, and the deviation is particularly large in the low-energy structures that result in a wrong energy ranking. On the other hand, the AtomFT result exhibits a good linear correlation for both the training and testing sets with the fitted line aligning closely with the diagonal. The RMSE value is 0.81 meV/atom for training and 0.98 meV/atom for testing, being less than one-tenth of the MBNN error.

Figure 5c further compares the energy spectrum for 95 low-energy conformations computed by DFT with PBE functional, MBNN, and AtomFT potentials, where all energies have been

corrected by Grimme D3 van der Waals energy.⁴⁷ These structures come from SSW global PES exploration in the 12-molecule supercell and are screened by energy and conformation from the SSW trajectories. As shown, DFT calculations correctly predict that the A phase has the lowest energy. The second lowest energy, B phase, is 0.237 eV (19.75 meV/molecule) less stable than the A phase from DFT and it has a $P\bar{1}$ space group with only 24 hydrogen bonds (Figure 5a), differing from the A phase in molecular rotation angles, arrangement, and lattice parameters (XYZ coordinates of A and B phases can be found in SI Part 5). In the AtomFT potential, the A phase and the B phase also have the lowest and the second lowest energy, respectively, whereas the MBNN potential ranks the A phase and B phase at the 58th and 18th positions, respectively. Quantitatively, we can utilize Spearman's rank correlation coefficient (ρ),⁴⁸ a nonparametric measure in statistics for the rank correlation, to quantify the correlation. The ρ is 0.985 between AtomFT and DFT, much higher than the 0.578 between MBNN and DFT.

It should be mentioned that the AtomFT potential can still be utilized for global optimization in general, the same as its baseline MBNN potential. Taking the same C–H–O–N-element systems, examples 2 and 3, we performed the cross-testing using AtomFT tuned for the chemical reactions (example 2) to explore the molecular crystal PES (example 3). It shows that the AtomFT performs similarly to the original MBNN for systems beyond the fine-tuning domain, as discussed in SI Part 6.

4. CONCLUSIONS

This work provides a low-cost solution to achieve highly accurate PES global exploration of a target system. This is via an AtomFT architecture, implemented on the commonly available CPU platform in LASP software, that can be utilized to fine-tune the global MBNN potential by exploiting the AFs of the MBNN outputs. Since the AFs are atom-based, the AtomFT potential, the same as the MBNN potential, is suitable for large-scale atomic simulations via the massive parallelization of atoms. We show that by iteratively updating the AFs, the fine-tuning module of AtomFT can perceive complex many-body information, which is cast into fine-tuning energy to correct the total energy.

Both the efficiency and accuracy of AtomFT have been systematically evaluated and carefully benchmarked on representative global PESs, where the accuracy from the MBNN potential remains unsatisfactory, including oxides with low defect content, molecular reactions, and molecular crystals. Our results demonstrate that the AtomFT architecture is a lightweight atomic simulation method, ideal for quickly solving challenging PES problems where the long-range interaction and/or the complex local many-body interactions are present. In all example systems, a PES accuracy of 1 meV/atom can be readily reached even with just one interaction block (NI = 1) in AtomFT. Since AtomFT bears similarities with the MPNN currently only implemented on GPU platform, we expect that the integration of global MLPs across different hardware platforms (CPU and GPU) is now ready technically, which, with the high accuracy level demonstrated here, will surely promote versatile applications of atomic simulations toward new findings.

■ ASSOCIATED CONTENT

SI Supporting Information

The Supporting Information is available free of charge at <https://pubs.acs.org/doi/10.1021/acs.jctc.5c00051>.

MB function parameters for Ti–O and C–H–O–N MBNN basis potentials; more information on the training of the MBNN basis potentials; accuracy of AtomFT with different NI; detailed benchmark results for molecular reactions; XYZ coordinates of A and B phases for the molecular crystal XXIX; cross-testing of AtomFT (PDF)

■ AUTHOR INFORMATION

Corresponding Authors

Cheng Shang – State Key Laboratory of Porous Materials for Separation and Conversion, Collaborative Innovation Center of Chemistry for Energy Material, Shanghai Key Laboratory of Molecular Catalysis and Innovative Materials, Key Laboratory of Computational Physical Science, Department of Chemistry, Fudan University, Shanghai 200433, China; orcid.org/0000-0001-7486-1514; Email: cshang@fudan.edu.cn

Zhi-Pan Liu – State Key Laboratory of Porous Materials for Separation and Conversion, Collaborative Innovation Center of Chemistry for Energy Material, Shanghai Key Laboratory of Molecular Catalysis and Innovative Materials, Key Laboratory of Computational Physical Science, Department of Chemistry, Fudan University, Shanghai 200433, China; State Key Laboratory of Metal Organic Chemistry, Shanghai Institute of Organic Chemistry, Chinese Academy of Sciences, Shanghai 200032, China; orcid.org/0000-0002-2906-5217; Email: zpliu@fudan.edu.cn

Authors

Xin-Tian Xie – State Key Laboratory of Porous Materials for Separation and Conversion, Collaborative Innovation Center of Chemistry for Energy Material, Shanghai Key Laboratory of Molecular Catalysis and Innovative Materials, Key Laboratory of Computational Physical Science, Department of Chemistry, Fudan University, Shanghai 200433, China; orcid.org/0009-0009-5166-2825

Tong Guan – State Key Laboratory of Porous Materials for Separation and Conversion, Collaborative Innovation Center of Chemistry for Energy Material, Shanghai Key Laboratory of Molecular Catalysis and Innovative Materials, Key Laboratory of Computational Physical Science, Department of Chemistry, Fudan University, Shanghai 200433, China

Zheng-Xin Yang – State Key Laboratory of Porous Materials for Separation and Conversion, Collaborative Innovation Center of Chemistry for Energy Material, Shanghai Key Laboratory of Molecular Catalysis and Innovative Materials, Key Laboratory of Computational Physical Science, Department of Chemistry, Fudan University, Shanghai 200433, China

Complete contact information is available at: <https://pubs.acs.org/doi/10.1021/acs.jctc.5c00051>

Notes

The authors declare no competing financial interest.

■ ACKNOWLEDGMENTS

This work was supported by the National Science Foundation of China (12188101, 22033003, 22122301, 92472113), the National Key Research and Development Program of China (2024YFA1509600), the Fundamental Research Funds for the Central Universities (20720220011), Science & Technology Commission of Shanghai Municipality (2024ZDSYS02), and the Tencent Foundation for XPLOER PRIZE.

■ REFERENCES

- (1) Kocer, E.; Ko, T. W.; Behler, J. Neural Network Potentials: A Concise Overview of Methods. *Annu. Rev. Phys. Chem.* **2022**, *73* (1), 163–186.
- (2) Wang, Y.; Wang, T.; Li, S.; He, X.; Li, M.; Wang, Z.; Zheng, N.; Shao, B.; Liu, T.-Y. Enhancing Geometric Representations for Molecules with Equivariant Vector-Scalar Interactive Message Passing. *Nat. Commun.* **2024**, *15* (1), 313.
- (3) Zhang, Y.; Xia, J.; Jiang, B. REANN: A PyTorch-Based End-to-End Multi-Functional Deep Neural Network Package for Molecular, Reactive, and Periodic Systems. *J. Chem. Phys.* **2022**, *156* (11), 114801.
- (4) Zubatyuk, R.; Smith, J. S.; Leszczynski, J.; Isayev, O. Accurate and Transferable Multitask Prediction of Chemical Properties with an Atoms-in-Molecules Neural Network. *Sci. Adv.* **2019**, *5* (8), No. eaav6490.
- (5) Zhang, L.; Han, J.; Wang, H.; Car, R.; E, W. Deep Potential Molecular Dynamics: A Scalable Model with the Accuracy of Quantum Mechanics. *Phys. Rev. Lett.* **2018**, *120* (14), No. 143001.
- (6) Jiang, B.; Guo, H. Permutation Invariant Polynomial Neural Network Approach to Fitting Potential Energy Surfaces. *J. Chem. Phys.* **2013**, *139* (5), No. 054112.
- (7) Behler, J.; Parrinello, M. Generalized Neural-Network Representation of High-Dimensional Potential-Energy Surfaces. *Phys. Rev. Lett.* **2007**, *98* (14), No. 146401.
- (8) Shao, K.; Chen, J.; Zhao, Z.; Zhang, D. H. Communication: Fitting Potential Energy Surfaces with Fundamental Invariant Neural Network. *J. Chem. Phys.* **2016**, *145* (7), No. 071101.
- (9) Smith, J. S.; Isayev, O.; Roitberg, A. E. ANI-1: An Extensible Neural Network Potential with DFT Accuracy at Force Field Computational Cost. *Chem. Sci.* **2017**, *8* (4), 3192–3203.
- (10) Schütt, K. T.; Sauceda, H. E.; Kindermans, P.-J.; Tkatchenko, A.; Müller, K.-R. SchNet – A Deep Learning Architecture for Molecules and Materials. *J. Chem. Phys.* **2018**, *148* (24), 241722.
- (11) Unke, O. T.; Meuwly, M. PhysNet: A Neural Network for Predicting Energies, Forces, Dipole Moments, and Partial Charges. *J. Chem. Theory Comput.* **2019**, *15* (6), 3678–3693.
- (12) Zhang, Y.; Hu, C.; Jiang, B. Embedded Atom Neural Network Potentials: Efficient and Accurate Machine Learning with a Physically Inspired Representation. *J. Phys. Chem. Lett.* **2019**, *10* (17), 4962–4967.
- (13) Zaverkin, V.; Holzmüller, D.; Steinwart, I.; Kästner, J. Fast and Sample-Efficient Interatomic Neural Network Potentials for Molecules and Materials Based on Gaussian Moments. *J. Chem. Theory Comput.* **2021**, *17* (10), 6658–6670.
- (14) Batzner, S.; Musaelian, A.; Sun, L.; Geiger, M.; Mailoa, J. P.; Kornbluth, M.; Molinari, N.; Smidt, T. E.; Kozinsky, B. E(3)-Equivariant Graph Neural Networks for Data-Efficient and Accurate Interatomic Potentials. *Nat. Commun.* **2022**, *13* (1), 2453.
- (15) Kovács, D. P.; Batatia, I.; Arany, E. S.; Csányi, G. Evaluation of the MACE Force Field Architecture: From Medicinal Chemistry to Materials Science. *J. Chem. Phys.* **2023**, *159* (4), No. 044118.
- (16) Kang, P.-L.; Yang, Z.-X.; Shang, C.; Liu, Z.-P. Global Neural Network Potential with Explicit Many-Body Functions for Improved Descriptions of Complex Potential Energy Surface. *J. Chem. Theory Comput.* **2023**, *19* (21), 7972–7981.
- (17) Musaelian, A.; Batzner, S.; Johansson, A.; Sun, L.; Owen, C. J.; Kornbluth, M.; Kozinsky, B. Learning Local Equivariant Representa-

tions for Large-Scale Atomistic Dynamics. *Nat. Commun.* **2023**, *14* (1), 579.

(18) Hong, C.; Kim, J.; Kim, J.; Jung, J.; Ju, S.; Choi, J. M.; Han, S. Applications and Training Sets of Machine Learning Potentials. *Science and Technology of Advanced Materials: Methods* **2023**, *3* (1), 2269948.

(19) Anstine, D. M.; Isayev, O. Machine Learning Interatomic Potentials and Long-Range Physics. *J. Phys. Chem. A* **2023**, *127* (11), 2417–2431.

(20) Yang, Y.; Zhang, S.; Ranasinghe, K. D.; Isayev, O.; Roitberg, A. E. Machine Learning of Reactive Potentials. *Annu. Rev. Phys. Chem.* **2024**, *75* (1), 371–395.

(21) Huang, S.-D.; Shang, C.; Zhang, X.-J.; Liu, Z.-P. Material Discovery by Combining Stochastic Surface Walking Global Optimization with a Neural Network. *Chem. Sci.* **2017**, *8* (9), 6327–6337.

(22) Huang, S.-D.; Shang, C.; Kang, P.-L.; Liu, Z.-P. Atomic Structure of Boron Resolved Using Machine Learning and Global Sampling. *Chem. Sci.* **2018**, *9* (46), 8644–8655.

(23) Huang, S.; Shang, C.; Kang, P.; Zhang, X.; Liu, Z. LASP: Fast Global Potential Energy Surface Exploration. *WIREs Comput. Mol. Sci.* **2019**, *9* (6), No. e1415.

(24) Kang, P.; Shang, C.; Liu, Z. Recent Implementations in LASP 3.0: Global Neural Network Potential with Multiple Elements and Better Long-Range Description. *Chinese Journal of Chemical Physics* **2021**, *34* (5), 583–590.

(25) Xie, X.-T.; Yang, Z.-X.; Chen, D.; Shi, Y.-F.; Kang, P.-L.; Ma, S.; Li, Y.-F.; Shang, C.; Liu, Z.-P. LASP to the Future of Atomic Simulation: Intelligence and Automation. *Precision Chemistry* **2024**, *2* (12), 612–627.

(26) Shang, C.; Liu, Z.-P. Stochastic Surface Walking Method for Structure Prediction and Pathway Searching. *J. Chem. Theory Comput.* **2013**, *9* (3), 1838–1845.

(27) Shang, C.; Zhang, X.-J.; Liu, Z.-P. Stochastic Surface Walking Method for Crystal Structure and Phase Transition Pathway Prediction. *Phys. Chem. Chem. Phys.* **2014**, *16* (33), 17845–17856.

(28) Kang, P.-L.; Shang, C.; Liu, Z.-P. Large-Scale Atomic Simulation via Machine Learning Potentials Constructed by Global Potential Energy Surface Exploration. *Acc. Chem. Res.* **2020**, *53* (10), 2119–2129.

(29) Zhang, K.-X.; Liu, Z.-P. *In Situ* Surfaced Mn–Mn Dimeric Sites Dictate CO Hydrogenation Activity and C₂ Selectivity over MnRh Binary Catalysts. *J. Am. Chem. Soc.* **2024**, *146* (39), 27138–27151.

(30) Chen, C.; Ong, S. P. A Universal Graph Deep Learning Interatomic Potential for the Periodic Table. *Nat. Comput. Sci.* **2022**, *2* (11), 718–728.

(31) Takamoto, S.; Shinagawa, C.; Motoki, D.; Nakago, K.; Li, W.; Kurata, I.; Watanabe, T.; Yayama, Y.; Iriguchi, H.; Asano, Y.; Onodera, T.; Ishii, T.; Kudo, T.; Ono, H.; Sawada, R.; Ishitani, R.; Ong, M.; Yamaguchi, T.; Kataoka, T.; Hayashi, A.; Charoenphakdee, N.; Ibuka, T. Towards Universal Neural Network Potential for Material Discovery Applicable to Arbitrary Combination of 45 Elements. *Nat. Commun.* **2022**, *13* (1), 2991.

(32) Deng, B.; Zhong, P.; Jun, K.; Riebesell, J.; Han, K.; Bartel, C. J.; Ceder, G. CHGNet as a Pretrained Universal Neural Network Potential for Charge-Informed Atomistic Modelling. *Nat. Mach. Intell.* **2023**, *5* (9), 1031–1041.

(33) Choudhary, K.; DeCost, B.; Major, L.; Butler, K.; Thiyagalingam, J.; Tavazza, F. Unified Graph Neural Network Force-Field for the Periodic Table: Solid State Applications. *Digital Discovery* **2023**, *2* (2), 346–355.

(34) Merchant, A.; Batzner, S.; Schoenholz, S. S.; Aykol, M.; Cheon, G.; Cubuk, E. D. Scaling Deep Learning for Materials Discovery. *Nature* **2023**, *624* (7990), 80–85.

(35) Batatia, I.; Benner, P.; Chiang, Y.; Elena, A. M.; Kovács, D. P.; Riebesell, J.; Advincula, X. R.; Asta, M.; Avaylon, M.; Baldwin, W. J.; Berger, F.; Bernstein, N.; Bhowmik, A.; Blau, S. M.; Cărare, V.; Darby, J. P.; De, S.; Pia, F. D.; Deringer, V. L.; Elijošius, R.; El-Machachi, Z.; Falcioni, F.; Fako, E.; Ferrari, A. C.; Genreith-Schriever, A.; George,

J.; Goodall, R. E. A.; Grey, C. P.; Grigorev, P.; Han, S.; Handley, W.; Heenen, H. H.; Hermansson, K.; Holm, C.; Jaafar, J.; Hofmann, S.; Jakob, K. S.; Jung, H.; Kapil, V.; Kaplan, A. D.; Karimiyari, N.; Kermodé, J. R.; Kroupa, N.; Kullgren, J.; Kumer, M. C.; Kuryla, D.; Liepuoniute, G.; Margraf, J. T.; Magdău, I.-B.; Michaelides, A.; Moore, J. H.; Naik, A. A.; Niblett, S. P.; Norwood, S. W.; O'Neill, N.; Ortner, C.; Persson, K. A.; Reuter, K.; Rosen, A. S.; Schaaf, L. L.; Schran, C.; Shi, B. X.; Sivonxay, E.; Stenczel, T. K.; Svahn, V.; Sutton, C.; Swinburne, T. D.; Tilly, J.; van der Oord, C.; Varga-Umbrich, E.; Vegge, T.; Vondrák, M.; Wang, Y.; Witt, W. C.; Zills, F.; Csányi, G. A Foundation Model for Atomistic Materials Chemistry. *arXiv* March 1, 2024. <http://arxiv.org/abs/2401.00096> (accessed 2024–10–11).

(36) Zhang, D.; Liu, X.; Zhang, X.; Zhang, C.; Cai, C.; Bi, H.; Du, Y.; Qin, X.; Peng, A.; Huang, J.; Li, B.; Shan, Y.; Zeng, J.; Zhang, Y.; Liu, S.; Li, Y.; Chang, J.; Wang, X.; Zhou, S.; Liu, J.; Luo, X.; Wang, J.; Jiang, W.; Wu, J.; Yang, Y.; Yang, J.; Yang, M.; Gong, F.-Q.; Zhang, L.; Shi, M.; Dai, F.-Z.; York, D. M.; Liu, S.; Zhu, T.; Zhong, Z.; Lv, J.; Cheng, J.; Jia, W.; Chen, M.; Ke, G.; E, W.; Zhang, L.; Wang, H. DPA-2: A Large Atomic Model as a Multi-Task Learner. *npj Comput. Mater.* **2024**, *10* (1), 293.

(37) Deng, B.; Choi, Y.; Zhong, P.; Riebesell, J.; Anand, S.; Li, Z.; Jun, K.; Persson, K. A.; Ceder, G. Systematic Softening in Universal Machine Learning Interatomic Potentials. *npj Comput. Mater.* **2025**, *11* (1), 9.

(38) Kang, P.; Shang, C.; Liu, Z. Recent Implementations in LASP 3.0: Global Neural Network Potential with Multiple Elements and Better Long-Range Description. *Chinese Journal of Chemical Physics* **2021**, *34* (5), 583–590.

(39) Scheiber, P.; Fidler, M.; Dulub, O.; Schmid, M.; Diebold, U.; Hou, W.; Aschauer, U.; Selloni, A. (Sub)Surface Mobility of Oxygen Vacancies at the TiO₂ Anatase (101) Surface. *Phys. Rev. Lett.* **2012**, *109* (13), No. 136103.

(40) Hoover, W. G. Canonical Dynamics: Equilibrium Phase-Space Distributions. *Phys. Rev. A* **1985**, *31* (3), 1695–1697.

(41) Shang, C.; Liu, Z.-P. Constrained Broyden Minimization Combined with the Dimer Method for Locating Transition State of Complex Reactions. *J. Chem. Theory Comput.* **2010**, *6* (4), 1136–1144.

(42) Zhang, X.-J.; Liu, Z.-P. Reaction Sampling and Reactivity Prediction Using the Stochastic Surface Walking Method. *Phys. Chem. Chem. Phys.* **2015**, *17* (4), 2757–2769.

(43) Zhang, X.-J.; Shang, C.; Liu, Z.-P. Double-Ended Surface Walking Method for Pathway Building and Transition State Location of Complex Reactions. *J. Chem. Theory Comput.* **2013**, *9* (12), 5745–5753.

(44) Eyring, H. The Activated Complex in Chemical Reactions. *J. Chem. Phys.* **1935**, *3* (2), 107–115.

(45) Hunnisett, L. M.; Nyman, J.; Francia, N.; Abraham, N. S.; Adjiman, C. S.; Aitipamula, S.; Alkhidir, T.; Almehairbi, M.; Anelli, A.; Anstine, D. M.; Anthony, J. E.; Arnold, J. E.; Bahrami, F.; Bellucci, M. A.; Bhardwaj, R. M.; Bier, I.; Bis, J. A.; Boese, A. D.; Bowskill, D. H.; Bramley, J.; Brandenburg, J. G.; Braun, D. E.; Butler, P. W. V.; Cadden, J.; Carino, S.; Chan, E. J.; Chang, C.; Cheng, B.; Clarke, S. M.; Coles, S. J.; Cooper, R. I.; Couch, R.; Cuadrado, R.; Darden, T.; Day, G. M.; Dietrich, H.; Ding, Y.; DiPasquale, A.; Dhokale, B.; Van Eijck, B. P.; Elsgood, M. R. J.; Firaha, D.; Fu, W.; Fukuzawa, K.; Glover, J.; Goto, H.; Greenwell, C.; Guo, R.; Harter, J.; Helfferich, J.; Hofmann, D. W. M.; Hoja, J.; Hone, J.; Hong, R.; Hutchison, G.; Ikabata, Y.; Isayev, O.; Ishaque, O.; Jain, V.; Jin, Y.; Jing, A.; Johnson, E. R.; Jones, I.; Jose, K. V. J.; Kabova, E. A.; Keates, A.; Kelly, P. F.; Khakimov, D.; Konstantinopoulos, S.; Kuleshova, L. N.; Li, H.; Lin, X.; List, A.; Liu, C.; Liu, Y. M.; Liu, Z.-P.; Lubach, J. W.; Marom, N.; Maryewski, A. A.; Matsui, H.; Mattei, A.; Mayo, R. A.; Melkumov, J. W.; Mohamed, S.; Momenzadeh Abardeh, Z.; Muddana, H. S.; Nakayama, N.; Nayal, K. S.; Neumann, M. A.; Nikhar, R.; Obata, S.; O'Connor, D.; Oganov, A. R.; Okuwaki, K.; Otero-de-la-Roza, A.; Pantelides, C. C.; Parkin, S.; Pickard, C. J.; Pilia, L.; Pivina, T.; Podeszwa, R.; Price, A. J. A.; Price, L. S.; Price, S. L.; Probert, M. R.; Pulido, A.; Ramekte, G. R.; Rehman, A. U.; Rezel-

Edens, S. M.; Rogal, J.; Ross, M. J.; Rumson, A. F.; Sadiq, G.; Saeed, Z. M.; Salimi, A.; Salvalaglio, M.; Sanders De Almada, L.; Sasikumar, K.; Sekharan, S.; Shang, C.; Shankland, K.; Shinohara, K.; Shi, B.; Shi, X.; Skillman, A. G.; Song, H.; Strasser, N.; Van De Streek, J.; Sugden, I. J.; Sun, G.; Szalewicz, K.; Tan, B. I.; Tan, L.; Tarczynski, F.; Taylor, C. R.; Tkatchenko, A.; Tom, R.; Tuckerman, M. E.; Utsumi, Y.; Vogt-Maranto, L.; Weatherston, J.; Wilkinson, L. J.; Willacy, R. D.; Wojtas, L.; Woollam, G. R.; Yang, Z.; Yonemochi, E.; Yue, X.; Zeng, Q.; Zhang, Y.; Zhou, T.; Zhou, Y.; Zubatyuk, R.; Cole, J. C. The Seventh Blind Test of Crystal Structure Prediction: Structure Generation Methods. *Acta Crystallogr., Sect. B: Struct. Sci., Cryst. Eng. Mater.* **2024**, *80* (6), 517.

(46) Ross, M.; Kabova, E.; Shankland, K. CCDC 2141426: *Experimental Crystal Structure Determination*. [10.5517/CCDC.CSD.CC29WB8T](https://doi.org/10.5517/CCDC.CSD.CC29WB8T).

(47) Grimme, S.; Antony, J.; Ehrlich, S.; Krieg, H. A Consistent and Accurate *Ab Initio* Parametrization of Density Functional Dispersion Correction (DFT-D) for the 94 Elements H-Pu. *J. Chem. Phys.* **2010**, *132* (15), 154104.

(48) Spearman, C. The Proof and Measurement of Association between Two Things. *American Journal of Psychology* **1904**, *15* (1), 72.